1-1-2014

A Transition Mass for Black Holes to Show Broad Emission Lines

Susmita Chakravorty
Harvard University

Martin Elvis
Harvard University

Gary J. Ferland
University of Kentucky, gary@uky.edu

Monthly Notices
of the
ROYAL ASTRONOMICAL SOCIETY

MNRAS **437,** 740–747 (2014)
Advance Access publication 2013 November 7

doi:10.1093/mnras/stt1930

A transition mass for black holes to show broad emission lines

Susmita Chakravorty,[1,2]★ Martin Elvis[2] and Gary Ferland[3]

[1]*Department of Astronomy, Harvard University, 60 Garden Street, Cambridge, MA 02138, USA*
[2]*Harvard–Smithsonian Center for Astrophysics, 60 Garden Street, Cambridge, MA 02138, USA*
[3]*Department of Physics and Astronomy, University of Kentucky, Lexington, KY 40506, USA*

Accepted 2013 October 7. Received 2013 October 7; in original form 2012 November 13

ABSTRACT

Although the supermassive (AGN) and stellar mass (BHBs) black holes have many properties in common, the broad emission lines (BELs) are exclusively signatures of the active galactic nuclei (AGN). Based on the detection of these lines from Sloan Digital Sky Survey (SDSS) data bases, there seems to be no AGN with mass $M_{\rm BH} \lesssim 10^5$ M$_\odot$. In this paper, we investigate if such low-mass black holes are really non-existent or they are undetected because the BELs in them are not produced efficiently. Using the ionizing spectral energy distribution for a wide range of black hole mass, 10–10^9 M$_\odot$, spanning black hole X-ray binaries (BHBs) to AGN, we calculate the equivalent widths (EWs) of ultraviolet and optical lines Lyα 1216 Å, Hβ 4861 Å, C IV 1549 Å and Mg II 2798 Å. The LOC (locally optimally emitting cloud) model has been used to describe the broad emission-line region (BELR) for the calculations. We find that the hardening of the SED shape with decreasing mass do not decrease the BEL EWs. However, finite size of the BELR, as measured by the line widths, which is controlled by the mass of the black hole, regulates the production of these emission lines. There seems to be a peak in the EWs of the emission lines for typical AGN black holes of $\sim 10^8$ M$_\odot$, below which the lines become intrinsically fainter with a sharp fall-off below $\sim 10^6$ M$_\odot$. This may be the cause of the absence of low-mass AGN in SDSS.

Key words: accretion, accretion discs – black hole physics – line: formation – galaxies: active – quasars: emission lines – galaxies: Seyfert.

1 INTRODUCTION

Active galactic nuclei (AGN) and black hole X-ray binaries (BHBs) share many properties, but broad emission lines (BELs) are not among them. One might speculate that the absence of BELs in BHB spectra may be due to the harder spectrum that is emitted by the accretion disc around the $\lesssim 10^6$ times smaller black holes. Here, we investigate the predicted BEL equivalent widths (EWs) over a wide range of black hole masses, 10–10^9 M$_\odot$ to see if there is a threshold mass below which BELs are not expected. The possibility of a threshold mass for strong BEL production has become interesting from recent observational results, which seem to suggest that there are no broad line emitting black holes below $M_{\rm BH} \lesssim 10^5$ M$_\odot$ (Greene & Ho 2004). Is this because there are no such black holes, or is it that, even when accreting at substantial rates, such black holes cannot produce BELs with detectable EWs?

Most existing photoionization calculations for the BELs in AGN, study the line strengths as a function of the overall shape of the ionizing continuum (Osterbrock & Ferland 2006; Leighly & Casebeer 2007) and the luminosity of the AGN. However, mostly, these studies do not take the further step of directly relating the emission-line properties to $M_{\rm BH}$ and $\dot{m}$. On the other hand, dynamical measurements of $M_{\rm BH}$, from the widths of the broad lines and/or using the reverberation mapping techniques (Peterson 1993; Netzer & Peterson 1997; Kaspi et al. 2000) consider an average $R_{\rm BELR} \sim L_{\rm AGN}^{1/2}$ relationship and do not need to delve into the details of the line strengths and ratios. In this study, we shall use the locally optimally emitting cloud (LOC) model, where the broad lines are due to locally, optimally emitting clouds, first suggested by Baldwin et al. (1995). We calculate the line strengths of the strongest broad lines, Lyα 1216 Å, Hβ 4861 Å, C IV 1549 Å and Mg II 2798 Å, as a function of the black hole mass ranging from 10 to 10^9 M$_\odot$.

2 THEORY

2.1 The accretion disc spectral energy distribution

A simple model for the radiation from the geometrically thin, optically thick accretion disc is a sum of local blackbodies emitted from

★ E-mail: write2susmita@gmail.com

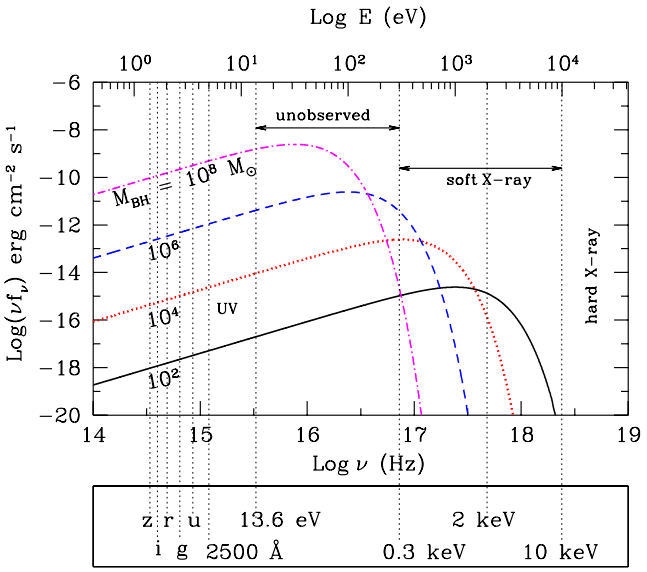

Figure 1. The SED from accretion discs around black holes of mass $M_{\rm BH} = 10^2$, 10^4, 10^6 and 10^8 $M_\odot$ accreting at $0.1\dot{m}_{\rm Edd}$ (or emitting at $0.1L_{\rm Edd}$). The absolute scale of the y-axis is arbitrary, assuming that all the sources are at a distance of 100 Mpc. However, the relative normalizations of the SEDs are according to their mass ratios. We have labelled some of the important energy values (accompanied by the dotted vertical lines) relevant for AGN SEDs. In particular, note the positions of the u (3551 Å), g(4686 Å), r(6165 Å), i(7481 Å) and z(8931 Å) filters used by the SDSS.

the different annuli of the disc at different radii. The temperature of the annulus at radius R is

$$T(R) = 6.3 \times 10^5 \left(\frac{\dot{m}}{\dot{m}_{\rm Edd}}\right)^{1/4} \left(\frac{M_{\rm BH}}{10^8\,{\rm M}_\odot}\right)^{-1/4} \left(\frac{R}{R_s}\right)^{-3/4} {\rm K} \quad (1)$$

(Peterson 1997; Frank, King & Raine 2002), where $\dot{m}$ is the accretion rate of the central black hole of mass $M_{\rm BH}$, $\dot{m}_{\rm Edd}$ is its Eddington accretion rate and $R_s = 2GM_{\rm BH}/c^2$ is the Schwarzschild radius (G is the gravitational constant and c is the velocity light). The normalization constant $A_{\rm dbb}$ for this spectral component is given by

$$A_{\rm dbb} = \left\{\frac{R_{\rm in}/{\rm km}}{D/(10\ {\rm kpc})}\right\}^2 \cos\theta \quad (2)$$

for an observer at a distance D whose line of sight makes and angle θ to the normal to the disc plane. $R_{\rm in}$ is the radial distance of the innermost stable annulus of the accretion disc from the black hole. $R_{\rm in}$ is assumed to be a $3R_s$ (as conventional).

A standard model for the above-mentioned spectral component from the accretion disc is available as disc blackbody (Mitsuda et al. 1984; Makishima et al. 1987) in XSPEC[1] (Arnaud 1996). We have used version 11.3 of XSPEC to generate the *disc blackbody* spectral component $f_{\rm dbb}(\nu)$ for $M_{\rm BH} = 10{-}10^9\,{\rm M}_\odot$ at steps of $\log(M_{\rm BH}/{\rm M}_\odot) = 0.5$ and $\dot{m} = 0.1\,\dot{m}_{\rm Edd}$ and $\theta = 30^\circ$ are held constant. The spectral energy distributions (SEDs) for $M_{\rm BH} = 10^2$, 10^4, 10^6 and 10^8 $M_\odot$ are shown in Fig. 1 to demonstrate how the peak of the SED and its normalization change as a function of the black hole mass. The SEDs for AGN with $M_{\rm BH} \geq 10^4$ $M_\odot$ peak in an energy range which is unobservable for extragalactic sources due to Galactic extinction. As a result, for AGN, determination of the mass of the black hole often depends on the study of the emission lines, particularly the BELs (Netzer 1987; Korista, Ferland & Baldwin 1997b; Kaspi et al. 2000; Bentz et al. 2006).

AGN are often selected from large data bases like Sloan Digital Sky Survey (hereafter SDSS) based on their broad-band optical colours, which depend on the intrinsic SED of the AGN. From Fig. 1, we see that all of the five SDSS filters (u-3551, g-4686, r-6165, i-7481 and z-8931 Å) are positioned on the linear, same slope 'low-energy' tail of the intrinsic AGN SEDs so that they cannot be distinguished as black holes of different mass, merely from studying the SDSS colours. SDSS, however, observes the redshifted and not the intrinsic SEDs of the quasars. Even when seeing the redshifted SED, there is no effect of the mass on the SDSS colours for $z < 8.60$ for $M_{\rm BH} \leq 10^6\,{\rm M}_\odot$.

We acknowledge that in the above argument we make a rather simplifying assumption that all AGN have the same slope in the optical energy band, i.e. all AGN have their optical SEDs defined by the low-energy tail of a 'diskbb' model. This assumption may not be strictly correct as discussed by Koratkar & Blaes (1999). More rigorous physical models of the accretion disc, considering radiative transfer through the atmosphere of the disc and/or the spin of the black hole, now exist (see Section 4 for further discussion on this issue). Further, the optical SED seen by us (SDSS) may not be merely the intrinsic accretion disc SED, and may have additional reprocessed light from outer parts of the AGN. However, it is beyond the scope of this paper to consider such complicated models. Our aim in this paper is to understand the relation between the black hole mass and the emission line strengths, for which we assume that all black holes have the same simplistic 'diskbb' model for an accretion disc SED. In our future publications, we shall address the effects of deviations from the 'diskbb' model.

Even if the colour selection algorithms of SDSS are not biased against detecting the lower mass black holes, they will still drop out because the intrinsic luminosity of the AGN decreases with the mass of the black hole. For example, based on the flux limits of the SDSS filters (Stoughton et al. 2002), the $M_{\rm BH} = 10^6\,{\rm M}_\odot$ black holes drop out beyond a redshift $z \geq 0.075$, whereas a $M_{\rm BH} = 10^8\,{\rm M}_\odot$ black hole can be seen for $z \leq 1.25$. Note that the aforementioned redshift limits are based on the continuum flux only. AGN are however detected primarily through the detection of their emission lines. The limits based on the emission lines would be different and we shall discuss this further in Section 3.

The SEDs described in this section are solely due to the radiation from the accretion disc around the black hole. Any observed broad-band AGN SED would show more spectral components than the radiation due to the accretion disc. For example, there is the power-law emission at higher energies ($\geq$500 eV) which may be due to inverse Comptonization of some of the disc photons by the hot coronal plasma surrounding the black hole. Moreover, for type I AGN, often an additional component, the soft-excess at $<$1 keV (often modelled as a blackbody of temperature 100−200 keV) is seen. However, for all the calculations presented in this paper, we ignore the power law and the soft-excess components of the SED. The energy range ($\lesssim$50 eV) of the AGN that influences the production and strength of the lines Hβ 4861 Å, C IV 1549 Å and Mg II 2798 Å are dominated by the disc emission for the black hole masses considered in this paper (e.g. at 30 eV the power law or the soft-excess would contribute less than 1 per cent of the radiation from the accretion disc around a black hole of $M_{\rm BH} \sim 10^8\,{\rm M}_\odot$). This issue is discussed again in greater detail in Section 4. Being thorough, we have in fact, investigated the effect of adding an X-ray power law to the accretion disc component (for black hole of $M_{\rm BH} \leq 10^8\,{\rm M}_\odot$)

[1] http://heasarc.gsfc.nasa.gov/docs/xanadu/xspec/

and found that there is no difference in the resultant line fluxes from when we consider an 'accretion disc only' SED.

2.2 The LOC model for the BELR

Baldwin et al. (1995) and Korista et al. (1997a) show that, for a given SED, any particular emission line is dominated by emission from a fairly narrow range of gas density ($n_{\rm H}$) and incident flux $\Phi(H) = Q(H)/4\pi R^2$, where $Q(H)$ is the number of hydrogen ionizing photons and R is the distance of the cloud from the source of the ionizing radiation. This narrow range of the $n_{\rm H}$ and $\Phi(H)$ is different for different emission lines. However, as long as there are enough clouds distributed over the relevant density and distance ranges, all the observed emission lines can be formed with the observed line ratios. This is thus, a model, which does not require any extreme fine tuning of $n_{\rm H}$ and $\Phi(H)$ to produce all the observed emission lines. Leighly & Casebeer (2007) discuss both the successes and limitations of the LOC model. Among limitations they mention that (a) some of the parameters of the model like the indices of the density and radial distribution of the clouds cannot be physically interpreted and (b) the model does not include some physical effects like self-shielding. An example of unsatisfactory LOC modelling is discussed for QSO J1546+5253 (Dhanda et al. 2007), where the authors attribute the discrepancies to unusual structure and/or unusual physical conditions in the broad emission-line region (BELR) of the object.

In this paper, we use the principles of the LOC model while calculating the average EW of the different emission lines. However, we make a modification by integrating the EWs across the column densities, as well. Our methods are discussed in details in Section 3.1.

3 CALCULATIONS

3.1 Unrestricted BELR

For each model SED, we use version C08.00 of CLOUDY[2] (Ferland et al. 1998), to calculate the emission-line spectrum for a three-dimensional parameter grid of $\Phi(H)$, $n_{\rm H}$ and column density ($N_{\rm H}$). $\log \Phi(H)$ is varied from 17 to 24 in steps of 0.5, $\log n_{\rm H}$ from 7 to 14 in steps of 0.5 and $\log N_{\rm H}$ from 21 to 23 in steps of 0.5, assuming a solar metallicity (Allende Prieto, Lambert & Asplund 2001, 2002; Holweger 2001; Grevesse & Sauval 1998) gas. We calculate the EWs of the 42 more prominent quasar emission lines (see Korista et al. 1997a, for the entire list). However, we demonstrate the results for only four of the strongest lines (Lyα 1216 Å, C IV 1549 Å, Mg II 2798 Å and Hβ 4861 Å) in this paper, which is adequate for the issues discussed here.

We assume solar metallicity for simplicity. The aforementioned four strong lines we use for demonstrating the science in this paper, do not have a significant metallicity dependence, as shown by Hamann & Ferland (1993, 1999). The 'thermostat effect' (Korista et al. 1998; Osterbrock & Ferland 2006) governs the intensities of strong lines in photoionization equilibrium. As metallicity increases, the gas cools more effectively and so the temperature falls resulting in constant intensity for the strong lines considered in this paper. Metallicity dependence is demonstrated by nitrogen lines because as Z increases, N/C or N/O increases as well (refer to Baldwin 1997, for a discussion). However, since we do not consider any such emission line in this paper, we can use solar metallicity gas for the simulations.

We plot the isocontours of the predicted EW (in log) for the 1549 Å C IV line in the $\log n_{\rm H} - \log \Phi(H)$ plane (Fig. 2) for the four SEDs with $M_{\rm BH} = 10^{2.0}$, $10^{4.0}$, $10^{6.0}$ and $10^{8.0}\,{\rm M}_\odot$. In the $\log \Phi(H) - \log n_{\rm H}$ plane, diagonal lines with a slope of 45° are lines of constant ionization parameter $U = \Phi(H)/cn_{\rm H}$, where the value of U increases from the bottom right to the top left. We see that the contours form well-defined diagonal ridges (collection of constant U lines) in the $\log \Phi(H) - \log n_{\rm H}$ plane with significant EW (>1). In each panel of Fig. 2, we have also labelled the limiting values of $\log U$, within which C IV line is efficiently produced with $1 \leq {\rm EW} \leq 10^{5.75}$ for $M_{\rm BH} = 10^{2.0}\,{\rm M}_\odot$, $1 \leq {\rm EW} \leq 10^{5.25}$ for $M_{\rm BH} = 10^{4.0}\,{\rm M}_\odot$, $1 \leq {\rm EW} \leq 10^{4.75}$ for $M_{\rm BH} = 10^{6.0}\,{\rm M}_\odot$, and $1 \leq {\rm EW} \leq 10^{3.75}$ for $M_{\rm BH} = 10^{8.0}\,{\rm M}_\odot$.

Deviations (of any contour) from the 45° lines show where thermal heating of the gas begins to be more important than photoionization, usually at high $n_{\rm H}$ and high $\Phi(H)$ (upper right, each panel). For example, taking the example of the $\log(EW) = 4$ contour for $M_{\rm BH} = 10^{2.0}\,{\rm M}_\odot$, we see that it 'turns over' from high $\log U(= -0.99$, $\log n_{\rm H} \geq 12$ and $\log \Phi(H) \geq 21.5)$ and becomes diagonal again at a lower $\log U(= -3.24)$.

To assess the sensitivity on column density, we have further drawn the EW isocontours for $\log N_{\rm H} = 21$ in Fig. 2 (dashed blue lines). The comparison with the $\log N_{\rm H} = 23$ show that at the low-ionization end the $\Phi(H) - n_{\rm H}$ distribution is identical, irrespective of the value of $N_{\rm H}$. It is only at the high-ionization end that the value of $N_{\rm H}$ makes any difference – emission lines from highly ionized clouds with low $N_{\rm H}$ ($\log N_{\rm H} = 21$) do not have sufficiently high EW ($\log({\rm EW}) \geq 0$). For example, the high-ionization ridge (upper left) is pushed to lower U by 1.23 dex for the $M_{\rm BH} = 10^{8.0}\,{\rm M}_\odot$ SED (see lower-right panel of Fig. 2). Thus, for any given SED, lower $N_{\rm H}$ restricts efficient line production to a tighter range of U.

To assess the contribution from all the clouds of different density, different column density and at different distances, we have taken a weighted average of EW:

$$\mathcal{EW} = f \iiint {\rm EW}(\Phi(H), n_{\rm H}, N_{\rm H}) \frac{{\rm d}\,\Phi(H)}{\Phi(H)} \frac{{\rm d}\,n_{\rm H}}{n_{\rm H}} \frac{{\rm d}\,N_{\rm H}}{N_{\rm H}} \qquad (3)$$

over $18 \leq \log \Phi(H) \leq 24$, $8 \leq \log n_{\rm H} \leq 14$ and $21 \leq \log N_{\rm H} \leq 23$, all in steps of 0.5. $f = 0.2$ is the constant covering fraction adopted in this paper.

Korista et al. (1997a), Baldwin (1997) and Bottorff et al. (2002) discuss the effect of varying R, $n_{\rm H}$ and $N_{\rm H}$ on the EWs of the emission lines. Baldwin (1997) summarizes that the integrated spectrum (i.e. the $\mathcal{EW}$s of emission lines) have a weak sensitivity to the radial and column density distribution of the clouds, as long as (a) $\gamma > -1$ in an R^γ radial distribution and (b) there are clouds with a wide range of R (through the range of $\Phi(H)$, in this paper) and $N_{\rm H}$. Baldwin (1997) further shows that a power-law index -1 is strongly suggested by observations for the density distribution. We accept the conclusions presented in the above-mentioned papers and use one constant value of -1 for slopes of the $\Phi(H)$, $n_{\rm H}$ and $N_{\rm H}$ distributions while performing our weighted integration to derive $\mathcal{EW}$.

Note that although Korista et al. (1997a) and Baldwin (1997) discuss the effect of column density on the EW contours, they leave out column density from the LOC integration of EWs and considered clouds of only $\log N_{\rm H}\ ({\rm cm}^{-2}) = 23$. In this paper, we have modified the standard method of LOC integration of EWs to integrate over $21 \geq \log N_{\rm H}\ ({\rm cm}^{-2}) \geq 23$, as well (equation 3). As shown in Fig. 2, the lower column densities would contribute EWs due to relatively

[2] URL: http://www.nublado.org/

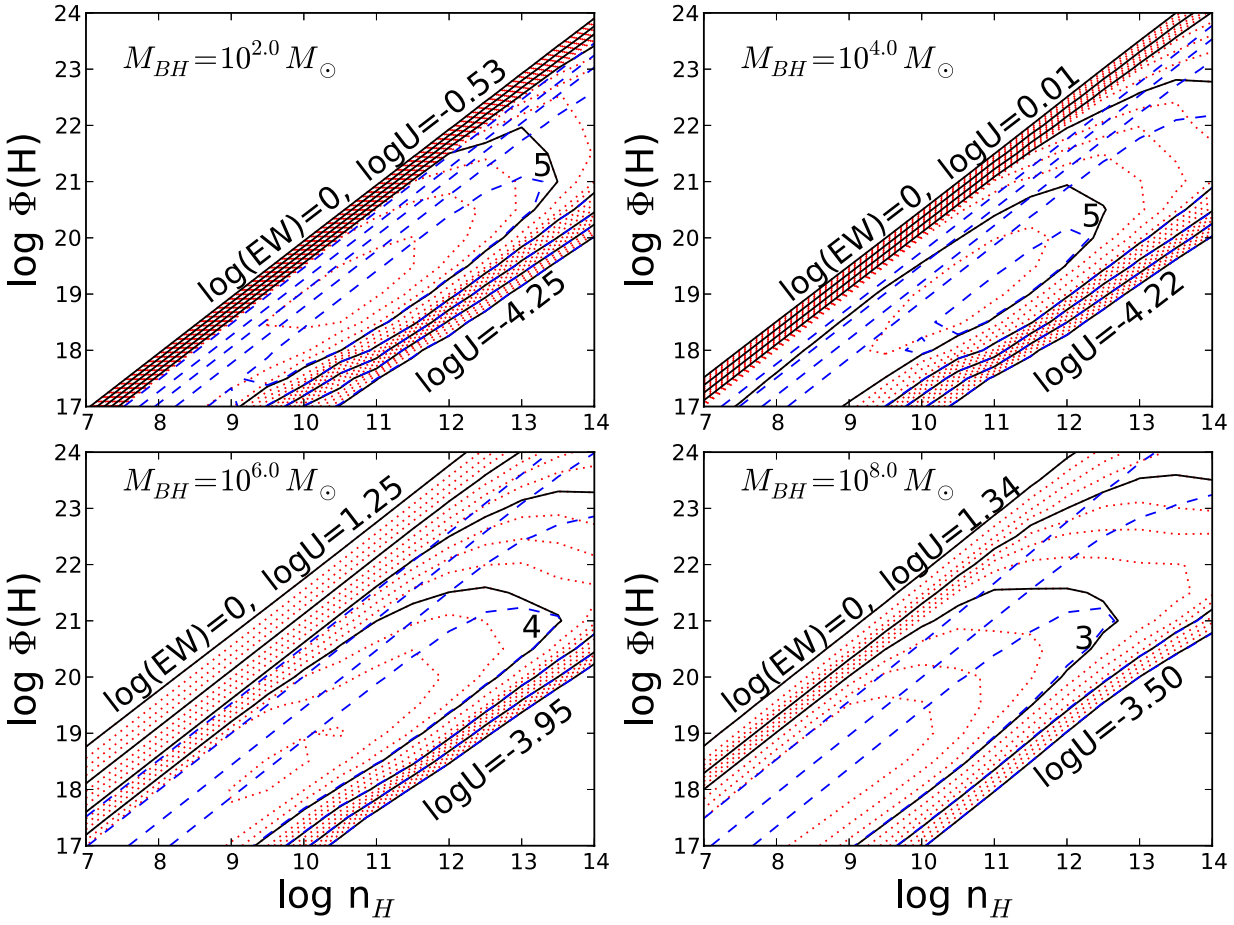

Figure 2. Contour plots for the C IV (1549 Å) EW as a function of the black hole mass in the $n_{\rm H}-\Phi(H)$ plane. The bold solid black lines are contours at steps of 1 dex and the intermediate dotted red lines are contours at steps of 0.25 dex, for $\log N_{\rm H} = 23$. In each panel, the outermost contours correspond to EW = 1 (log(EW) = 0), whereas the innermost contours of the maximum EW are different for different SEDs due to different black hole mass. Note that diagonal lines with a slope of 45° in the $\log\Phi(H)-\log n_{\rm H}$ plane are lines of constant ionization parameter $U = \Phi(H)/cn_{\rm H}$. In each panel, we have labelled the value of $\log U$ corresponding to the outermost EW = 1 contour, both at the low-ionization and high-ionization end. For comparison, we also over plot the isocontours for $\log N_{\rm H} = 21$ (dashed blue lines) at steps of 1 dex, the outermost contour being for log(EW) = 0.

lower ionization parameters. The −1 slope of the $N_{\rm H}$ distribution, used in (equation 3) further facilitates the contribution from the lower $N_{\rm H}$ clouds. The overall effect of including the column density as a variable in the EW integration is to increase the resultant $\mathcal{EW}$ by a factor of a few. For example, for the black hole of mass $M_{\rm BH} = 10^{8.0}\,{\rm M}_\odot$, $\mathcal{EW}$ for C IV 1549 Å is higher by a factor of 1.28 when the integration includes column density as a variable.

$\mathcal{EW}$ (in log) as a function of $M_{\rm BH}$ for Lyα, C IV, Mg II and Hβ is shown in Fig. 3 (dotted black line). For each of the emission lines, the average $\mathcal{EW}$ rises monotonically with the decrease in mass. We further calculate the line ratios Mg II/C IV and Mg II/Hβ and plot them against each other in Fig. 4 (dotted black line). The labelled solid black circles along the line mark the black hole masses in units of $\log(M_{\rm BH}/\,{\rm M}_\odot)$.

3.2 Restriction on the radius of the BELR

3.2.1 Limits from velocity of the clouds

Reverberation mapping has established that the time lag between the variation in the continuum flux and the line flux $t_{\rm lag}$ is proportional to 1/2 power of the full width at half-maxima (FWHM; see Bentz et al. 2006, and references therein). Hence, the BELR gas seems to move with Keplerian or at least virialized velocities, so that we can define the outermost radius of the BELR

$$R_{\rm Keplerian} = G\,M_{\rm BH}/v_{\rm min}^2 \qquad (4)$$

corresponding to the clouds with the lowest observed velocity $v_{\rm min}$. The FWHM of BEL are $\gtrsim$2000(>1200) km s^{-1} (Hao et al. 2005), so that $v_{\rm min}(=\,{\rm FWHM}/\sqrt{8\ln 2}) \gtrsim 1000\,{\rm km\,s^{-1}}$. The distribution of $R_{\rm Keplerian}$ are shown as solid red lines in Fig. 5, for $v_{\rm min}$ = 1000, 3000 and 10 000 km s^{-1}.

Introducing an $R_{\rm Keplerian}$ cut-off in our CLOUDY simulations, produces a pronounced cut-off in $\mathcal{EW}$ (solid red lines in Fig. 3). BELs used by SDSS to detect and identify AGN activity, Hβ 4861 Å, C IV 1549 Å and Mg II 2798 Å are all affected. The ratio $\mathcal{EW}_{7.5}/\mathcal{EW}_{5.0} > 10$ for all the emission lines, for $v_{\rm min} = 3000\,{\rm km\,s^{-1}}$ (Table 1, bottom panel of Fig. 6), where $\mathcal{EW}_x$ is the $\mathcal{EW}$ due to the black hole mass $M_{\rm BH} = 10^x\,{\rm M}_\odot$. This ratio is as high as 720 for Mg II 2798 Å. Below $M_{\rm BH} = 10^{5.0}\,{\rm M}_\odot$, $\mathcal{EW}$ rapidly falls for all the lines.

The larger BELR allowed by $v_{\rm min} = 1000\,{\rm km\,s^{-1}}$ produces a less drastic drop and theory predicts non-zero EWs up to much lower black hole masses ($\sim 10^{2.5}\,{\rm M}_\odot$). For $v_{\rm min} = 1000\,{\rm km\,s^{-1}}$, $\mathcal{EW}_{7.5}/\mathcal{EW}_{5.0}$ reduces to 5.27 for Mg II 2798 Å. Table 1 list the EW ratios for the different lines and the same are plotted in the top

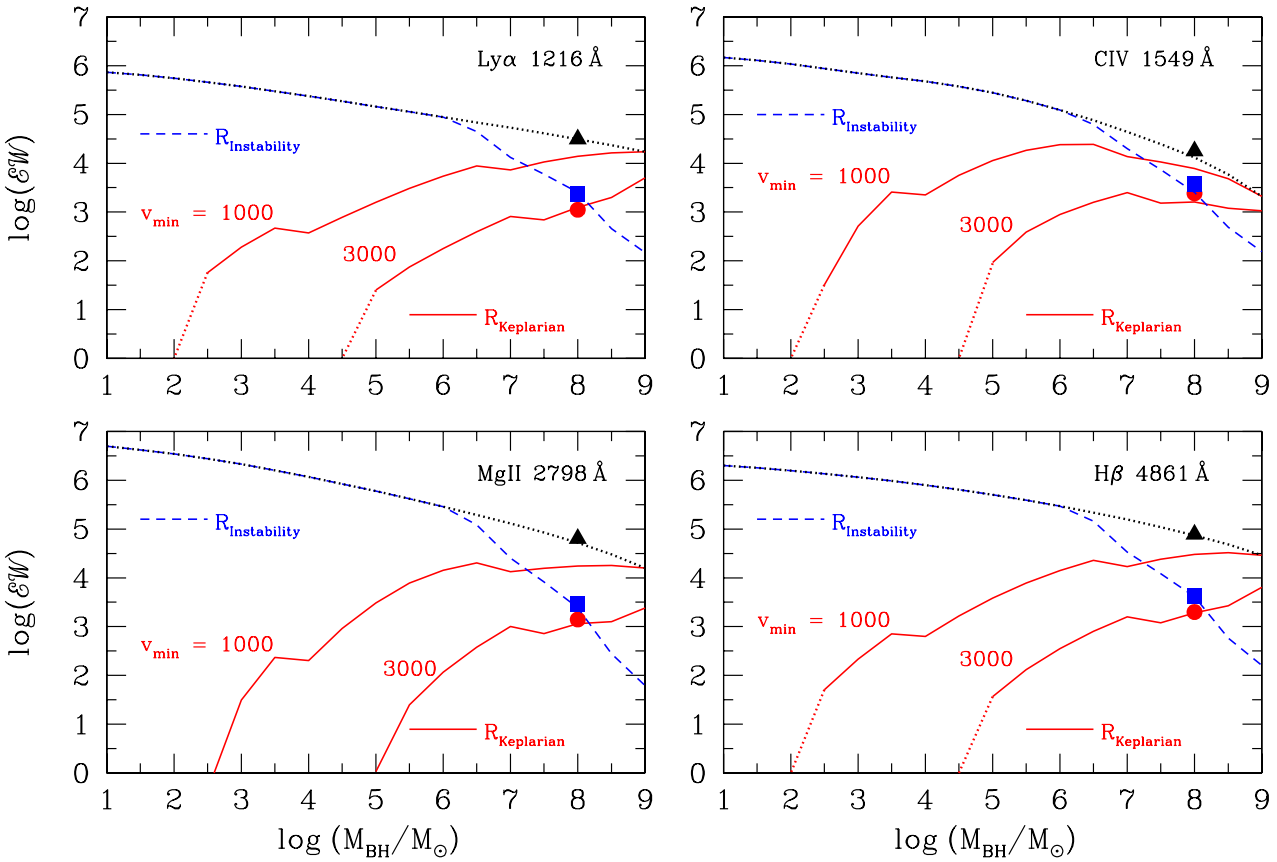

Figure 3. The weighted average ($\mathcal{EW}$) for four of the strongest broad lines, as a function of black hole mass is given by the dotted black line in each panel. The filled black triangle at $M_{\rm BH} = 10^{8.0}\,{\rm M}_{\odot}$ shows the value of $\mathcal{EW}$ if we consider an SED with a disc blackbody plus an X-ray power law, instead of just a disc blackbody SED. The mass distribution of $\mathcal{EW}$ is modified if a cut-off is applied on the maximum allowed radius of the BELR; the solid red curves (with different minimum velocity of the BELR clouds, in $\rm km\,s^{-1}$) if the cut-off is determined using Keplerian mechanics (equation 4) and the dashed blue curve if the cut-off is determined from the considerations of the gravitational instability radius of the accretion disc (equation 5). The filled red circle and the filled blue square denote the value of $\mathcal{EW}$ for the disk+power-law SED for $M_{\rm BH} = 10^{8.0}\,{\rm M}_{\odot}$ when the respective radius cut-off schemes (as described above) are assumed. Note that for the Keplerian cut-off mechanism, we have shown the filled circle only for the $v_{\rm min} = 3000\,{\rm km\,s^{-1}}$ case.

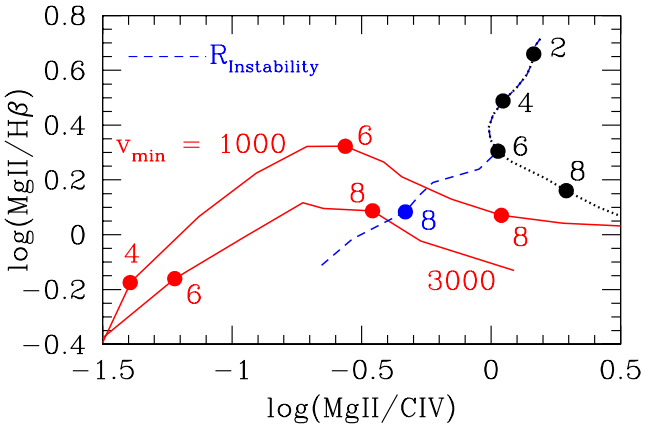

Figure 4. The line ratios Mg II/C IV and Mg II/Hβ are plotted against each other for the three different BELR. The case of Unrestricted BELR (Section 3.1), with no upper limits on its size, is represented by the dotted black line. When the BELR is truncated using limits from observed Keplerian velocities (Section 3.2) we have line ratio profiles given by the solid red lines, for the two different velocities of the clouds, namely, $v_{\rm min} = 1000$ and $3000\,{\rm km\,s^{-1}}$. The dashed blue line corresponds to BELR with size limitations imposed by the gravitational instability (Section 3.2.2). The solid circles represent the points on the line ratio profiles for different black hole masses (as labelled) in units of $\log(M_{\rm BH}/{\rm M}_{\odot})$.

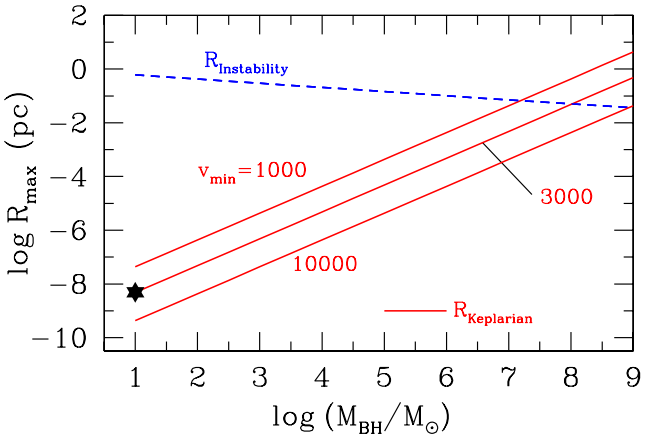

Figure 5. The outer radius of BELR as a function of black hole mass. Various methods of determining this cut-off radius are demonstrated : considering (a) a phenomenological approach based on the observed velocities of the emission lines (solid red lines) and (b) gravitational instability of the accretion disc (dashed blue line). For stellar mass black hole ($M_{\rm BH} = 10\,{\rm M}_{\odot}$), the black star shows the tidal disruption radius.

Table 1. The ratio of the weighted EWs $\mathcal{EW}$ for different black hole masses. We have considered the finite size of the BELR, cut-off corresponding to the two Keplerian velocities $v_{\rm min} = 3000$ and $1000\ {\rm km\,s^{-1}}$.

Cut-off used ($v_{\rm min}$ km s^{-1})	C IV−1549Å		Mg II−2798Å		Hβ−4861Å	
	$\frac{\mathcal{EW}_{7.5}}{\mathcal{EW}_{4.0}}$	$\frac{\mathcal{EW}_{7.5}}{\mathcal{EW}_{5.0}}$	$\frac{\mathcal{EW}_{7.5}}{\mathcal{EW}_{4.0}}$	$\frac{\mathcal{EW}_{7.5}}{\mathcal{EW}_{5.0}}$	$\frac{\mathcal{EW}_{7.5}}{\mathcal{EW}_{4.0}}$	$\frac{\mathcal{EW}_{7.5}}{\mathcal{EW}_{5.0}}$
3000	–	17.52	–	720	–	32.22
1000	4.83	0.96	79.31	5.27	39.37	6.27

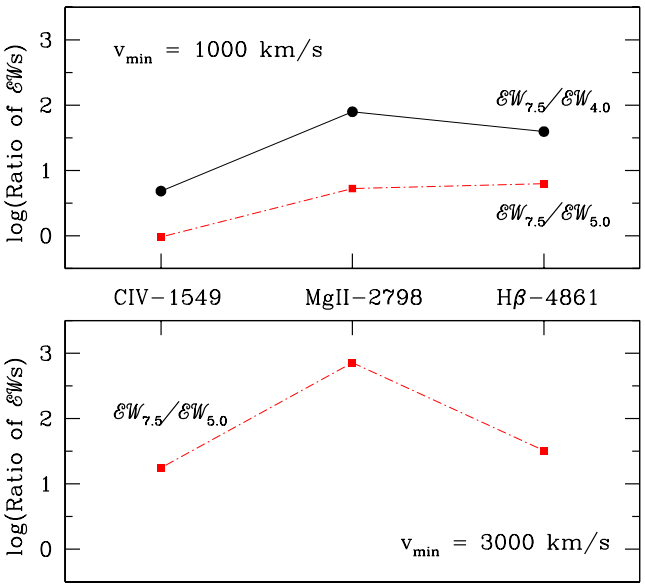

Figure 6. The ratios (in log) of the weighted EWs $\mathcal{EW}$ for the three different emission lines Mg II 2798 Å and Hβ 4861 Å. We have considered the finite size of the BELR, cut-off corresponding to the two Keplerian velocities $v_{\rm min} = 1000$ (top panel) and 3000 (bottom panel) km s^{-1}.

panel of Fig. 6. In fact, for the two C IV and Mg II lines the $\mathcal{EW}$ profiles are not monotonically decreasing functions of black hole mass, rather the peak of the profiles shift to lower mass $\sim 10^{6.5}\,{\rm M}_\odot$.

The intrinsic luminosity in the lines depends on the mass of the black hole. For example, for an unrestricted BELR (dotted black lines in Fig. 3) around a $10^6\,{\rm M}_\odot$ black hole, we convert $\mathcal{EW}_{6.0}$ to intrinsic luminosity for Mg II 2798 Å and Hβ 4861 Å. The predicted theoretical luminosity is such that the Mg II 2798 Å line should be detected up to a redshift of 0.67 and the Hβ 4861 Å line up to 0.27 by SDSS (according to the central wavelength and detection limits of the filters, given by Stoughton et al. 2002). However, SDSS surveys do not find $10^6\,{\rm M}_\odot$ black holes using these emission lines, at the above-mentioned redshifts. We found that this disparity between our predictions and the lack of SDSS observations can be mitigated if we instead, consider BELRs with size limitations. For example, the predicted luminosities of Mg II 2798 Å or Hβ 4861 Å for a size limited BELR around a $10^6\,{\rm M}_\odot$ black hole (for both $v_{\rm min} = 1000$ and $3000\,{\rm km\,s^{-1}}$, solid red lines in Fig. 3) are low enough that they should not be detected by SDSS.

The line ratios Mg II/Hβ versus Mg II/C IV, for the size-limited BELR, using Keplerian cut-offs, are plotted using the solid red lines in Fig. 4. The distribution of Mg II/Hβ as functions of Mg II/C IV are very different from the case of the unrestricted BELR (dotted black line). For a $10^8\,{\rm M}_\odot$, the values for the line ratio Mg II/Hβ are almost same for the size limited and the unrestricted BELR, but the line ratio Mg II/C IV is very different in the two cases. This line ratio varies from the unrestricted BELR case by 0.25 dex for $v_{\rm min} = 1000\,{\rm km\,s^{-1}}$ and by 0.74 dex for $v_{\rm min} = 3000\,{\rm km\,s^{-1}}$. For a $10^6\,{\rm M}_\odot$, black, even the Mg II/Hβ ratio varies from the unrestricted BELR case by 0.47 dex in the $v_{\rm min} = 3000\,{\rm km\,s^{-1}}$ limited BELR. The Mg II/C IV line ratio varies from the unrestricted BELR case by 0.59 dex for $v_{\rm min} = 1000\,{\rm km\,s^{-1}}$ and by 1.24 dex for $v_{\rm min} = 3000\,{\rm km\,s^{-1}}$. Such variations in the line ratios for different physical scenarios of the BELR, would act as diagnostics in our future publications when we shall compare our theoretical results with observations from SDSS or the likes of it, not only for these three emission lines, but for many more appropriately chosen BELs.

3.2.2 *Gravitational disc instability*

The outer parts of a geometrically thin and optically thick accretion disc becomes self-gravitating and breaks up. This radius has been suggested as the outer boundary of the BELR and the beginning of the 'torus' (Netzer & Laor 1993; Collin & Hure 2001; Suganuma et al. 2006). The radius at which the disc becomes Toomre unstable (the Toomre parameter; $Q < 1$ Binney & Tremaine 1987) depends weekly on the central black hole mass. Translating the Toomre criterion in terms of the α-disc parameters, $\Sigma/H = M_{\rm BH}/R^3_{\rm Instability}$ (Σ is the surface density and H is the scaleheight of the disc), gives us

$$R^{-9/8}_{\rm Instability} = 1.31 \times 10^{21} \alpha^{-7/10}_{\rm disc} \left(\frac{\dot{m}}{\dot{m}_{\rm Edd}}\right)^{11/20} \left(\frac{M_{\rm BH}}{{\rm M}_\odot}\right)^{7/40} f^{11/5} \tag{5}$$

(Frank et al. 2002), where $R_{\rm Instability}$ is in cm. $\alpha_{\rm disc}$ is the free parameter associated with the subsonic turbulent viscosity of a thin accretion disc and varies between zero (for no accretion) and approximately 1. $f^4 = 1 - (\frac{6GM_{\rm BH}}{{\rm M}_\odot})^{1/2}$. The much weaker mass evolution of $R_{\rm Instability}$ (compared to $R_{\rm Keplerian}$) is shown as a dashed blue line in Fig. 5 for $\alpha_{\rm disc} = 0.1$ and $\dot{m} = 0.1\dot{m}_{\rm Edd}$.

Using the $R_{\rm Instability}$ cut off, below $M_{\rm BH} \sim 10^{6.0}\,{\rm M}_\odot$, the $\mathcal{EW}$ distribution is same as when no radius restriction is applied, leading to the unobserved increase in $\mathcal{EW}$ with decreasing mass (dashed blue curves in Fig. 3). The line corresponding to line ratios Mg II/Hβ versus Mg II/C IV are shown by the dashed blue line in Fig. 4, further showing that the line fluxes are exactly the same as that for an unrestricted BELR for $M_{\rm BH} <= 10^{6.0}\,{\rm M}_\odot$

3.2.3 *Tidal disruption by stellar mass black holes*

In the previous sections of this paper, we have discussed emission line strengths from gas around black holes of a wide range of masses, including ones with $M_{\rm BH}$ as low as $10\,{\rm M}_\odot$ (e.g. see Fig. 3). For these low stellar mass black holes, the above-mentioned 'gravitational disc instability' is not relevant. On the other hand, the accretion disc around such black holes is more likely to suffer tidal disruption. In this section, we briefly discuss the tidal disruption caused by a $10\,{\rm M}_\odot$ black hole and calculate the radius of disruption, to put it in the context of the other radii discussed in Sections 3.2.1 and 3.2.2.

According to Hills (1975) and Gezari et al. (2003),

$$R_{\rm Tidal} = 1.1 R_{\rm sch} \left(M_{\rm BH}/10^8\,{\rm M}_\odot\right)^{-2/3}, \tag{6}$$

for solar mass disrupted stars. Thus, the disruption does not happen for $M_{\rm BH} > 1.1 \times 10^8\,{\rm M}_\odot$ – the stars are swallowed whole. Thus, we use (equation 6) to calculate $R_{\rm Tidal}$ for a black hole of $M_{\rm BH} = 10\,{\rm M}_\odot$ having a solar mass binary companion. The tidal disruption

is plotted as a black star in Fig. 5, and we find that $R_{\rm Tidal} \sim R_{\rm Keplerian}$ for $v_{\rm min} = 3000$. Our calculations for $\mathcal{EW}$ suggest zero flux in the emission lines for such low-mass black holes (see Fig. 3) when the BELR size limit is imposed with $v_{\rm min} = 3000\,{\rm km\,s^{-1}}$. No high-sensitivity search for these emission lines have been conducted for stellar mass black holes to corroborate or contradict these theoretical results.

4 DISCUSSION AND FUTURE WORK

(i) Additional components of the AGN SED:
Both the AGN (supermassive black holes) and the BHBs (solar mass black holes) are powered by the active matter accretion into the black hole. However, the emission from the accretion disc is not the only component of the observed SED from the AGN or the BHBs. In both cases, we also observe power-law emission at higher energies ($\geq$500 eV for AGN and $\geq$3 keV for BHBs). The power law is thought to be due to inverse Comptonization of some of the disc photons by the hot coronal plasma surrounding the black hole, or due to the jet (particularly for BHBs). In the case of AGN of type 1, sometimes we see an additional component, the soft-excess at $<$1 keV, which may be Comptonized disc emission or an entirely separate component altogether. Often the soft-excess can be modelled as a blackbody of temperature 100–200 keV. However, for all the calculations presented in this paper, we ignore the power-law and the soft-excess components of the SED, because their shape or strength are independent of the mass of the black hole.

The strengths of the emission lines from the X^ith ions are determined by the available number of photons close to the ionization potential (IP) of the X^{i-1}th ions. In this paper, we have restricted our studies to black holes with $M_{\rm BH} \lesssim 10^9\,{\rm M_\odot}$ because it was sufficient to consider only the mass dependent accretion disc component of the SED. In this mass range, the accretion disc is hot enough that the energy ranges of the ionization or excitation potentials ($\lesssim$50 eV) required to produce the lines Hβ 4861 Å, C IV 1549 Å and Mg II 2798 Å are dominated by the disc emission and the power law or the soft-excess would contribute less than 1 per cent of the radiation from the accretion disc.

To be thorough, we investigated the effect of adding an X-ray power law with spectral index $\alpha = 0.8$ and $\alpha_{\rm OX} = 1.2$ for $M_{\rm BH} = 10^{8.0}\,{\rm M_\odot}$. In each panel of Fig. 3, the resultant $\mathcal{EW}$s are shown as filled black triangles, for an unrestricted BELR, as filled red circle for the $v_{\rm min} = 3000\,{\rm km\,s^{-1}}$ Keplerian limit on the BELR and as filled blue squares for the BELR restricted by gravitational instability. In each case, these points lie exactly on the line for the $\mathcal{EW}$ distribution, generated using only the accretion disc component, showing that the addition of the power-law and the soft-excess component is redundant for these emission lines in the black hole mass range considered. We would like to note here that Korista et al. (1997b) had pointed out the deficiency of enough $E > 54.4$ eV (IP of He II) photons in the SED of the quasar Mrk 335 to produce the observed He II emission lines strengths. Although not shown in the figures of this paper, we have calculated and compared $\mathcal{EW}$ for He II 1640 Å using the 'accretion disc only' SED (which is the default in this paper) with the case when the additional X-ray power-law component is added to the SED, for $M_{\rm BH} = 10^{8.0}\,{\rm M_\odot}$. As for H$\beta$ 4861 Å, C IV 1549 Å and Mg II 2798 Å, $\mathcal{EW}$ for He II 1640 Å came out to be equal in the two cases.
However, while considering similar studies for higher mass black holes, one has to carefully account for the other aforementioned components of the AGN SED because, the high-energy tail of the accretion disc SED for $M_{\rm BH} >= 10^9\,{\rm M_\odot}$ may cut-off at less than $\sim$50 eV.
Similar considerations are required for constructing the AGN SED required to correctly predict the $\mathcal{EW}$ for O VI 1034 Å, which is an important BEL in the UV. The IP of OV is 113.90 eV, an energy range dominated by the power law for quasar-like ($M_{\rm BH} \gtrsim 10^{8.0}\,{\rm M_\odot}$) SED. Thus, $\mathcal{EW}$ calculations for OVI would require an AGN SED including all the components, and not just the accretion disc emission. We will study such emission lines in details in our future publications.

(ii) Alternative models for the accretion disc:
Instead of a radiatively efficient, thin accretion disc (modelled by 'diskbb' in this paper, hereafter BBB), sometimes black holes might have advection dominated, radiatively inefficient accretion flows, which would result in significantly different SEDs (see e.g. Hopkins et al. 2009) than the models considered in this paper. These alternative prescriptions drastically change the shape of the SED in the energy range of the IP of the ions responsible for the BELs and the narrow emission lines (NELs). We intend to calculate the line strengths due to such ionizing SEDs and predict observable signatures, which might act as diagnostic tools.

Even for the BBB, more rigorous models exist for modelling the radiation from the accretion disc (BBB). For example, Blaes et al. (2001), Hubeny et al. (2000, 2001), Hui, Krolik & Hubeny (2005) discuss the role of real radiative transfer in the accretion disc. The spin of the black hole is another physical parameter parameter to be considered (Davis et al. 2005; Davis & Hubeny 2006). Qualitatively speaking, for the same black hole mass and accretion rate, these models push the peak of the SED to higher energies than due to the 'diskbb' model. We would like to calculate line strengths corresponding to these models and test if the observations of BELs and NELs are sensitive enough to differentiate these accretion disc models from BBB.

(iii) Comparison with data:
We intend to use the SDSS data base for Hβ 4861 Å, C IV 1549 Å and Mg II 2798 Å and the *HST* and/or *FUSE* data base for O VI 1034 Å, to compare our predicted $\mathcal{EW}$ and line ratios with the observed line strengths. We would hope to draw constraints on other physical parameters (e.g. distance of the BELR) by such comparisons. Eventually, we would want to extend our theoretical analysis to include other fundamental black hole parameters like the accretion rate. We would like to test if such systematic LOC modelling can explain observed effects like the 'Baldwin Effect' (Baldwin 1977), where the EW of the C IV emission line decreases with increasing continuum luminosity.

(iv) Narrow emission lines:
We intend to do similar studies for the NELs in the AGN spectrum. It would be interesting to see if they also show a mass dependence of the $\mathcal{EW}$, given that the NEL clouds are further away from the black hole and may be outside its sphere of influence (FWHM for NEL 1/6 of that for BELs) and/or their sizes are not governed by Keplerian dynamics.

5 CONCLUSIONS

(i) We wanted to investigate if there is a lower mass cut-off below which black holes cannot produce the BELs like Hβ 4861 Å, C IV 1549 Å and Mg II 2798 Å typically used to detect and identify AGN activity from large optical data bases like the SDSS.

(ii) Using the standard LOC (locally optically emitting clouds) model for the BELR without any restrictions on the radius on its

radius, photoionization calculations show an unobserved rise in the equivalent widths ($\mathcal{EW}$s) of the lines with decreasing mass.

(iii) However, introducing a cut-off radius for the BELR produces sharp mass-dependent drops in the $\mathcal{EW}$s, when the cut-off radius is determined from simple Keplerian mechanics, depending on the mass of the black hole ($M_{\rm BH}$). Such drops are consistent with the observations including that below $M_{\rm BH} = 10^5\,{\rm M}_{\odot}$ the above-mentioned emission lines are not observed. Our findings conclude that these observations may not indicate the absence of black holes of such low mass, but the inability of such black holes to produce the observable (with our detectors) line strengths.

(iv) Such a conclusion might have consequences for modifying the black hole mass function in the lower mass end. However, before we can attempt to address such issues, we need to carry out a more rigorous systematic study (listed above, in Section 4) of the $\mathcal{EW}$ of BELs and NELs, as a function of other fundamental black hole parameters like its accretion rate and alternative accretion theory models.

ACKNOWLEDGEMENTS

SC thanks Aneta Siemiginowska, Hans Moritz Guenther, Nirupam Roy and Yue Shen for helpful discussions and tips. We gratefully acknowledge the use of the Cosmology Calculator (Wright 2006). GJF acknowledges support by NSF (1108928 and 1109061), NASA (10-ATP10-0053, 10-ADAP10-0073 and NNX12AH73G), and STScI (HST-AR-12125.01, GO-12560 and HST-GO-12309). SC gratefully thanks Prof. Karl Menten and acknowledges the support provided by Max Planck Institut fur Radioastronomie.

REFERENCES

Allende Prieto C., Lambert D. L., Asplund M., 2001, ApJ, 556, L63
Allende Prieto C., Lambert D. L., Asplund M., 2002, ApJ, 573, L137
Arnaud K. A., 1996, in Jacoby G. H., Barnes J., eds, ASP Conf. Ser. 101, Astronomical Data Analysis Software and Systems V. Astron. Soc. Pac., San Francisco, p. 17
Baldwin J. A., 1977, ApJ, 214, 679
Baldwin J. A., 1997, in Peterson B. M., Cheng F., Wilson A. S., eds, ASP Conf. Ser. 113, Emission Lines in Active Galaxies: New Methods and Techniques. Astron. Soc. Pac., San Francisco, p. 80
Baldwin J. A., Ferland G., Korista K., Verner D., 1995, ApJ, 455, L119
Bentz M. C., Peterson B. M., Pogge R. W., Vestergaard M., Onken C. A., 2006, ApJ, 644, 133
Binney J., Tremaine S., 1987, Galactic Dynamics. Princeton Univ. Press, Princeton, NJ
Blaes O., Hubeny I., Agol E., Krolik J. H., 2001, ApJ, 563, 560
Bottorff M. C., Baldwin J. A., Ferland G., Ferguson J. W., Korista K. T., 2002, ApJ, 581, 932
Collin S., Hure J. M., 2001, A&A, 372, 50
Davis S. W., Hubeny I., 2006, ApJS, 164, 530
Davis S. W., Blaes O. M., Hubeny I., Turner N. J., 2005, ApJ, 621, 372
Dhanda N., Baldwin J. A., Bentz M. C., Osmer P. S., 2007, ApJ, 658, 804
Ferland G. J., Korista K. T., Verner D. A., Ferguson J. W., Kingdon J. B., Verner E. M., 1998, PASP, 110, 761
Frank J., King A., Raine D. J., 2002, Accretion Power in Astrophysics. Cambridge Univ. Press, Cambridge
Gezari S., Halpern J. P., Komossa S., Grupe D., Leighly K. M., 2003, ApJ, 592, 42
Greene J. E., Ho L. C., 2004, ApJ, 610, 722
Grevesse N., Sauval A. J., 1998, Space Sci. Rev., 85, 161
Hamann F., Ferland G., 1993, ApJ, 418, 11
Hamann F., Ferland G., 1999, ARA&A, 37, 487
Hao L. et al., 2005, ApJ, 129, 1783
Hills J. G., 1975, Nat, 254, 295
Holweger H., 2001, in Wimmer-Schweingruber R. F., ed., AIP Conf. Proc., Vol. 598, Solar and Galactic Composition. Am. Inst. Phys., New York, p. 23
Hopkins P. F., Hickox R., Quataert E., Hernquist L., 2009, MNRAS, 398, 333
Hubeny I., Agol E., Blaes O., Krolik J. H., 2000, ApJ, 533, 710
Hubeny I., Blaes O., Krolik J. H., Agol E., 2001, ApJ, 559, 680
Hui Y., Krolik J. H., Hubeny I., 2005, ApJ, 625, 913
Kaspi S., Smith P. S., Netzer H., Maoz D., Jannuzi B. T., Giveon U., 2000, AJ, 533, 631
Koratkar A., Blaes O., 1999, PASP, 111, 1
Korista K., Baldwin J., Ferland G., Verner D., 1997a, ApJS, 108, 401
Korista K., Ferland G., Baldwin J., 1997b, ApJ, 487, 555
Korista K., Baldwin J., Ferland G., Verner D., 1998, ApJ, 507, 24
Leighly K. M., Casebeer D., 2007, in Ho L. C., Wang J.-M., eds, ASP Conf. Ser. 373, The Central Engine of Active Galactic Nuclei. Astron. Soc. Pac., San Francisco, p. 365
Makishima K., Maejima Y., Mitsuda K., Bradt H. V., Remillard R. A., Tuohy I. R., Hoshi R., Nakagawa M., 1986, ApJ, 308, 635
Mitsuda K. et al., 1984, PASJ, 36, 741
Netzer H., 1987, MNRAS, 225, 55
Netzer H., Laor A., 1993, ApJ, 404, L51
Netzer H., Peterson B. M., 1997, in Maoz D., Sternberg A., Leibowitz E., eds, Astronomical Time Series. Kluwer, Dordrecht, p. 85
Osterbrock D. E., Ferland G. J., 2006, Astrophysics of Gaseous Nebulae and Active Galactic Nuclei. University Science Books, Mill Valley, CA
Peterson B. M., 1993, PASP, 105, 207
Peterson B. M., 1997, An Introduction to Active Galactic Nuclei. Cambridge Univ. Press, Cambridge
Stoughton C. et al., 2002, AJ, 123, 485
Suganuma M. et al., 2006, ApJ, 639, 46
Wright E. L., 2006, PASP, 118, 1711

This paper has been typeset from a TEX/LATEX file prepared by the author.